



Tuning magnetic correlations in $s = 1/2$ spin ladder $\text{Ba}_2\text{CuTe}_{1-x}\text{W}_x\text{O}_6$ through site-selective cation substitution

Muskan Sande , Joydev Khatua, Youngsu Choi,* and Kwang-Yong Choi [†]

Department of Physics, Sungkyunkwan University, 2066 Seobu-ro, Suwon, Republic of Korea



(Received 9 April 2024; accepted 21 August 2024; published 6 September 2024)

The site-selective substitution of diamagnetic d^{10}/d^0 cations offers an efficient way to fine-tune magnetic characteristics by controlling orbital hybridization and superexchange pathways. Herein, we explore the tunability of magnetic properties in coupled spin-ladder compounds $\text{Ba}_2\text{CuTe}_{1-x}\text{W}_x\text{O}_6$ ($x = 0.0 - 0.30$). The pristine compound exhibits spin-singlet correlations at elevated temperatures, as evidenced by a magnetic susceptibility peak at $T_{\text{max}} \sim 70$ K, Schottky-like specific heat, unconventional magnetic Raman scattering, and a quasilinear decrease in the electron spin resonance linewidth. Notably, the substitution of W^{6+} for Te^{6+} brings about several marked changes: an increase in the Curie-Weiss temperature, a suppression in the Néel ordering temperature, enhanced magnetic susceptibility at low temperatures, and a weakening of spin-ladder correlations. These modifications collectively suggest that the newly activated exchange interactions through W^{6+} substitution primarily alter intraladder spin topology while amplifying quantum critical fluctuations. This finding highlights the potential for controlling magnetic correlations in spin-ladder compounds through targeted chemical substitution.

DOI: [10.1103/PhysRevMaterials.8.094404](https://doi.org/10.1103/PhysRevMaterials.8.094404)

I. INTRODUCTION

Spin ladder systems, characterized by their unique quasi-one-dimensional arrangement of magnetic ions networked through leg (J_{leg}) and rung (J_{rung}) couplings, have provided a fertile ground for exploring a variety of emergent quantum phenomena including Tomonaga-Luttinger liquids, magnon fractionalization, unconventional superconductivity, and quasiparticle confinement [1–5]. One of the pivotal strategies for manipulating and tailoring the distinct physical properties of these ladder systems is chemical substitution. This approach allows for the tuning of structural, electronic, and magnetic properties without the need for external control parameters such as temperature, pressure, or magnetic fields. Specifically, by adjusting the $J_{\text{leg}}/J_{\text{rung}}$ ratio, the elementary excitations of two-leg spin ladders can vary from triplons to pairs of bound spinons [6].

In this pursuit, $\text{A}_2\text{B}'\text{B}''\text{O}_6$ double perovskite oxides have garnered significant interest due to their exceptional tunability, which is rooted in the rich array of compositional variations among A, B', and B'' elements. Here, B' represents a magnetic cation, and B'' denotes a diamagnetic cation with either a d^{10} or d^0 electronic configuration [7,8]. The double perovskite structure comprises alternating layers of corner-sharing B'O₆ and B''O₆ octahedra arranged in a rocksalt-type pattern. Magnetic interactions are mediated through superexchange paths B'-O-B''-O-B', involving the orbital overlap between the d^{10}/d^0 orbitals of B'' cations and the 2p orbitals of oxygen [9].

In this exchange topology, the distinct electronic configurations of B'' cations enable specific types of superexchange interactions [9–13]. Notably, B'-O-B''-O-B' superexchange pathways are effective only for $5d^0$ B'' cations due to strong orbital hybridization with the O 2p orbitals in the valence band. Conversely, for $4d^{10}$ cations, B'-O-O-B' superexchange pathways are predominant as the $4d^{10}$ orbitals, lying well below the Fermi level, hinder hybridization with the O 2p orbitals. The strategic substitution of diamagnetic d^{10} and d^0 cations into extended superexchange pathways has been demonstrated in B-site ordered double perovskites $\text{Sr}_2\text{Cu}(\text{Te}_{1-x}\text{W}_x)\text{O}_6$, which embody an $s = 1/2$ square-lattice Heisenberg J_1 - J_2 model [14–20]. Here, J_1 and J_2 represent nearest-neighbor and next-nearest-neighbor exchange interactions along a side and a diagonal of the square, respectively. Through W-for-Te substitution, J_2 interactions (180° Cu-O-W-O-Cu superexchange paths) become enhanced relative to J_1 interactions (90° Cu-O-O-Cu pathways). The increased magnetic frustration engenders a quantum spin liquid state and a random singlet state over a wide compositional range of $x \approx 0.05 - 0.6$ [11,12,17–20], showcasing the potential of compositional tuning in bringing about novel quantum states.

Subsequently, the effects of d^{10}/d^0 substitution have been expanded to hexagonal perovskites $\text{Ba}_2\text{CuTe}_{1-x}\text{W}_x\text{O}_6$ [21]. Unlike the double perovskite structure, Cu^{2+} cations in hexagonal perovskites are linked through either corner-sharing Te(1)O₆ or face-sharing Te(2)O₆ octahedra, as sketched in Fig. 1. This structural peculiarity realizes a two-leg spin ladder in the pristine compound $\text{Ba}_2\text{CuTeO}_6$, which consists of nearly isotropic intraladder interactions with $J_{\text{leg}} \approx J_{\text{rung}} \approx 90$ K [22–31]. The presence of weak interladder J_{inter} interactions induces a long-range magnetic order at $T_N = 15$ K. Nonetheless, spin-ladder correlations at elevated temperatures remain observable, as evidenced by a broad maximum around

*Contact author: youngsu.c@skku.edu[†]Contact author: choisky99@skku.edu

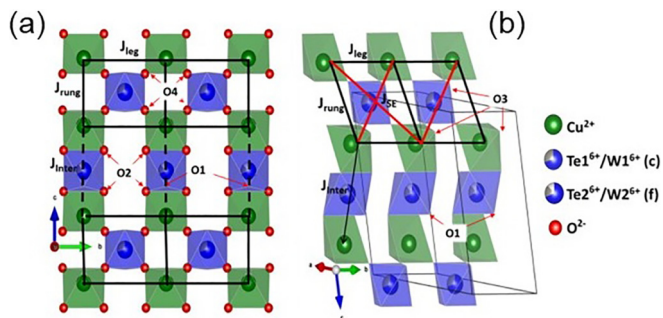


FIG. 1. (a) Crystal structure and projected view of $\text{Ba}_2\text{CuTe}_{1-x}\text{W}_x\text{O}_6$ along the a axis. The green, blue/gray, and red spheres represent Cu, Te/W, and O ions, respectively. The Ba atoms are omitted to enhance visibility. The CuO_6 octahedra are interconnected through either face-shared $\text{Te}(2)\text{O}_6(\text{f})$ or corner-shared $\text{Te}(1)\text{O}_6(\text{c})$, leading to the formation of coupled spin ladders. The solid lines denote the leg J_{leg} and rung J_{rung} couplings, while the dashed lines indicate the interactions between ladders (J_{inter} coupling). (b) Modification of exchange interactions when W^{6+} ions replace Te^{6+} ions. The red solid lines stand for newly activated diagonal interactions (J_{SE}) through Cu-O4-W1-O4-Cu superexchange paths, which are absent for Te^{6+} ions.

70 K in magnetic susceptibility along with largely hidden thermodynamic signatures of magnetic ordering, and unconventional magnetic scattering probed by Raman spectroscopy. Upon substituting W^{6+} for Te^{6+} in $\text{Ba}_2\text{CuTe}_{1-x}\text{W}_x\text{O}_6$, both synchrotron x-ray and extended x-ray absorption fine structure reveal that the W^{6+} cations preferentially occupy corner-sharing sites, thereby primarily affecting the strengths of intraladder interactions [21]. This site-specific substitution is purported to lead to a dimensional reduction from a spin ladder to a more one-dimensional spin chain.

In this paper, we have successfully synthesized a series of $\text{Ba}_2\text{CuTe}_{1-x}\text{W}_x\text{O}_6$ ($x = 0 - 0.3$) powder samples and investigated the effects of W^{6+} substitution on magnetism through thermodynamic, electron spin resonance, and Raman scattering measurements. Our comparative analysis indicates that spin-ladder-like correlations diminish with increasing x , suggesting an intriguing modification in the underlying coupled spin-ladder network. We discuss the possible origins of this altered spin dynamics in terms of newly created diagonal interactions within spin ladder topology.

II. EXPERIMENTAL DETAILS

A series of polycrystalline samples of $\text{Ba}_2\text{CuTe}_{1-x}\text{W}_x\text{O}_6$ ($x = 0 - 0.3$) was synthesized using solid-state reactions. Stoichiometric amounts of high-purity BaCO_3 (99.997%), CuO (99.9995%), WO_3 (99.99%), and TeO_2 (99.997%) powders were ground in an agate mortar. The mixture was pressed into pellets and calcinated at 900°C for 12 h before heating at 1100°C for 24 h. This process was repeated with intermittent grinding to achieve phase purity for all samples. The phase purity of the obtained samples was confirmed through powder x-ray diffraction (XRD) analysis conducted with a Bruker D8 ADVANCE phaser diffractometer, utilizing Cu- $K\alpha$ radiation ($\lambda = 1.5405 \text{ \AA}$). The XRD data were analyzed using Rietveld refinement as implemented in the FULLPROF software

[32]. The powder samples changed color from light yellow to darker shades with increasing W^{6+} concentration, showing their successful incorporation into the lattice.

Magnetic susceptibility was measured using a vibrating sample magnetometer option of Physical Properties Measurement System (PPMS; Quantum Design Dynacool) over a temperature range of $T = 2 - 300$ K in an external magnetic field of $\mu_0 H = 0.1$ T. Heat-capacity measurements were performed using a Quantum Design PPMS instrument with the thermal relaxation method over the $T = 2 - 300$ K temperature range. For specific-heat measurements, $\text{Ba}_2\text{CuTe}_{1-x}\text{W}_x\text{O}_6$ samples were compacted into pellets and sliced into small pieces (of dimension $3 \times 3 \times 3 \text{ mm}^3$) weighing approximately 1.1–3.4 mg each.

Electron spin resonance (ESR) spectra were measured using a conventional X-band spectrometer (Bruker Elexsys EMX ESR900) at a microwave frequency of $\nu \approx 9.8$ GHz. The temperature was varied between 5 and 300 K with a continuous He-flow cryostat (ESR900, Oxford Instruments). Temperature-dependent Raman scattering measurements were conducted using a micro-Raman spectrometer (XperRam200VN, NanoBase) equipped with an air-cooled charge-coupled device (Andor iVac Camera). The laser beam ($\lambda = 532 \text{ nm}$; $P = 1.5 \text{ W}$) was focused on the sample surface using a $40\times$ magnification microscope objective. A notch filter was utilized to reject Rayleigh scattering below 15 cm^{-1} . The samples were placed in a continuous helium-flow cryostat, enabling measurements within a temperature range of $T = 5 - 300$ K. We note that the ESR and Raman measurements for the $x = 0.3$ concentration level were not conducted due to a shortage of liquid helium during the experiments. Nonetheless, the key physics of this study remains unaltered.

III. RESULTS AND DISCUSSION

A. Crystal structure and lattice parameters

To determine the lattice parameters of polycrystalline samples of $\text{Ba}_2\text{CuTe}_{1-x}\text{W}_x\text{O}_6$ ($x = 0 - 0.3$), Rietveld refinement was made on powder XRD data. The Rietveld refinement confirmed that all studied samples crystallize in the identical space group $C2/m$ (see Tables III–VI in the Appendix), in agreement with previous work [21]. As shown in the resulting refinement pattern in Fig. 2, we detected no impurity phases, corroborating the successful synthesis of W-substituted samples in their single phase. The Rietveld refinement results for the powder XRD data, including the lattice parameters, are provided in Figs. 3(a)–3(e) and the Appendix.

As plotted in Figs. 3(a)–3(e), we observe a linear decrease in the lattice parameters for the a , b , and c axes, as well as the unit cell volume (V) and monoclinic angle (β) with an increase in x . This observation complies with Vegard's law, indicating the effective substitution of W^{6+} ions into the $\text{Ba}_2\text{CuTeO}_6$ structure, consistent with prior reports [21].

In Figs. 3(f)–3(l) and Table I, we detail the bond distances and angles of superexchange paths between two adjacent Cu^{2+} spins: three distinct intraladder interactions including the rung (J_{rung}), leg (J_{leg}), and diagonal (J_{SE}) interactions, and one interladder interaction (J_{inter}). As the W^{6+} concentration increases, the bond distances of Cu-O4(=O4-Cu),

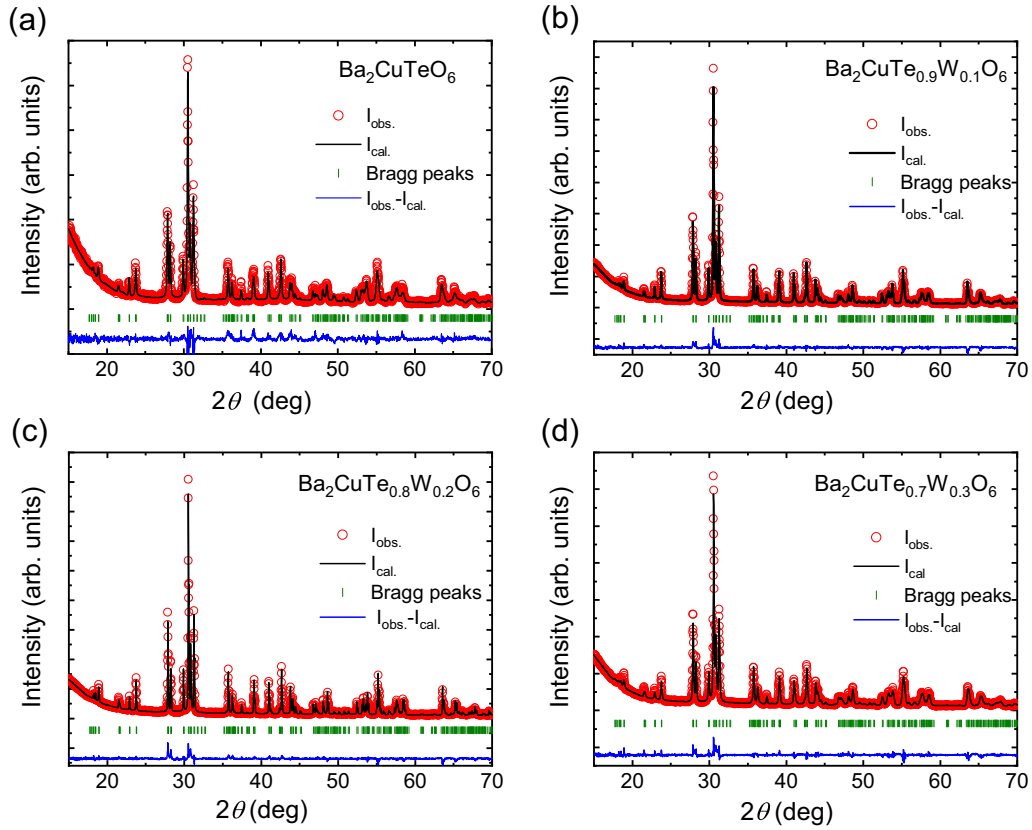


FIG. 2. Rietveld refinement pattern of powder x-ray diffraction data for the series of $\text{Ba}_2\text{CuTe}_{1-x}\text{W}_x\text{O}_6$ for $x = 0$ (a), 0.1 (b), 0.2 (c), and 0.3 (d) measured at room temperature. The red circles, black line, olive vertical bars, and blue line represent the experimentally observed points, the Rietveld fitting curve, theoretical Bragg reflection positions, and the difference between observed and calculated intensities, respectively.

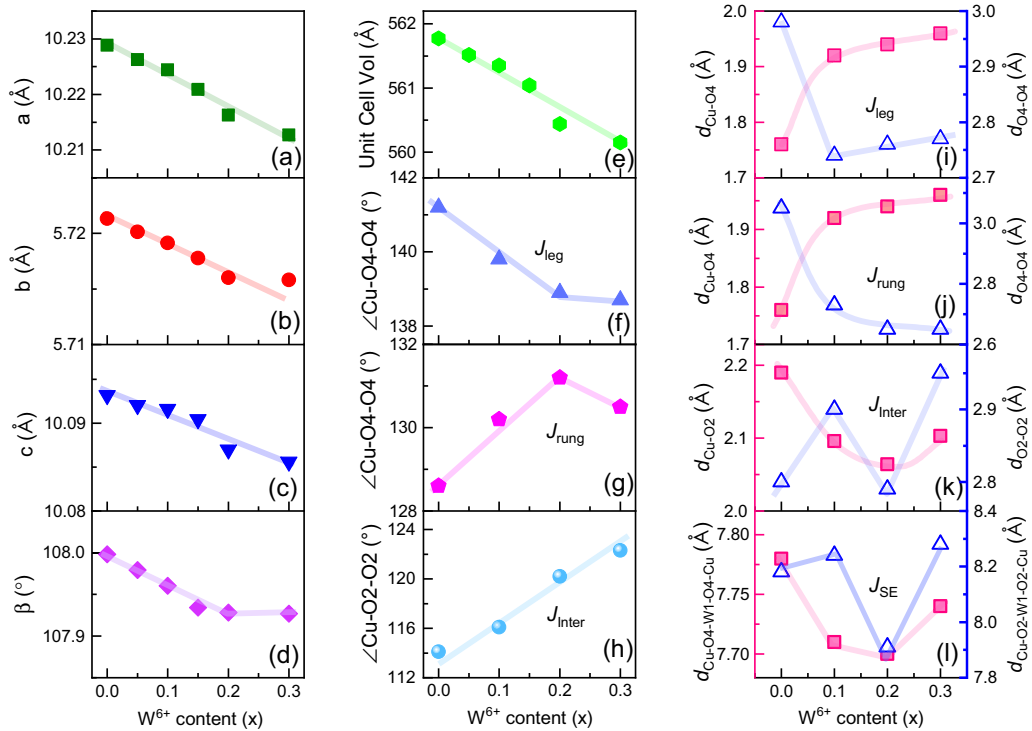


FIG. 3. (a)–(c) Unit cell parameters, (d) monoclinic angle β , and (e) unit cell volume as a function of x in the monoclinic phase ($C2/m$). (f)–(h) Bond angles of superexchange paths vs x for J_{leg} , J_{rung} , and J_{inter} , respectively. (i)–(l) Bonding distances vs x , mediating the J_{leg} , J_{rung} , J_{inter} , and J_{SE} interactions. The errors are not larger than the symbol size. Thick solid lines serve as a linear guide for the eye.

TABLE I. Bond distances and angles of superexchange paths between two neighboring Cu^{2+} spins, primarily resulting in modifications of four exchange interactions.

Superexchange paths	$x = 0.0$	$x = 0.1$	$x = 0.2$	$x = 0.3$	
J_{leg}	(Cu-O4 = O4-Cu)	1.76 Å	1.92 Å	1.94 Å	1.96 Å
	O4-O4	2.98 Å	2.74 Å	2.76 Å	2.77 Å
	($\angle\text{Cu-O4-O4} = \angle\text{O4-O4-Cu}$)	141.2°	139.8°	138.9°	138.7°
J_{rung}	(Cu-O4 = O4-Cu)	1.76 Å	1.92 Å	1.94 Å	1.96 Å
	(O4-O4)	3.05 Å	2.73 Å	2.65 Å	2.65 Å
	($\angle\text{Cu-O4-O4} = \angle\text{O4-O4-Cu}$)	128.6°	130.2°	131.2°	130.5°
J_{SE}	(Cu-O4-Te1/W1-O4-Cu)	7.78 Å	7.71 Å	7.70 Å	7.74 Å
	(Cu-O2-Te2/W2-O2-Cu)	8.18 Å	8.24 Å	7.91 Å	8.28 Å
	(Cu-O2 = O2-Cu)	2.19 Å	2.09 Å	2.06 Å	2.10 Å
J_{Inter}	O2-O2	2.80 Å	2.90 Å	2.79 Å	2.95 Å
	($\angle\text{Cu-O2-O2} = \angle\text{O2-O2-Cu}$)	114.1°	116.1°	120.2°	122.3°

mediating both J_{rung} and J_{leg} , are expanded, whereas the bond distance between O4-O4 contracts [Figs. 3(i) and 3(j)]. Overall, the distances $d_{\text{Cu-Cu}}$ involving J_{leg} and J_{rung} vary little with x . On the other hand, the bond angles of $\angle\text{Cu-O4-O4}$ ($=\angle\text{O4-O4-Cu}$) show an opposite trend: $\angle\text{Cu-O4-O4}$ involving J_{leg} diminishes with increasing x [Fig. 3(f)], while $\angle\text{Cu-O4-O4}$ of J_{rung} becomes larger [Fig. 3(g)]. According to the Goodenough-Kanamori-Anderson rule, the strength of J_{rung} is enhanced with increasing x , while the J_{leg} interaction is somewhat reduced. We observe no apparent trend for the distances Cu-O2(=O2-Cu) and O2-O2, which mediate the J_{Inter} interaction [Fig. 3(k)]. Conversely, the bond angle of $\angle\text{Cu-O2-O2}$ increases gradually with an increase in W^{6+} concentration [Fig. 3(h)]. Based on this observation, we infer that the strength of J_{Inter} increases moderately upon W^{6+} substitution. In addition, the J_{SE} interactions (180° Cu-O4-W1-O4-Cu paths), which are negligible for the pristine sample, are newly activated thanks to the strong orbital hybridization of $5d^0$ W^{6+} cations with the O $2p$ orbitals. It is noteworthy that the W^{6+} substitution effect is to generate spin tetrahedral clusters [marked by the red lines in Fig. 1(b)] embedded within the coupled spin ladders. Here, four spin triangles formed by the J_{rung} , J_{leg} , and J_{SE} interactions are topologically equivalent to a spin tetrahedron. Consequently, the inclusion of these zero-dimensional frustrated spin tetrahedra is anticipated to enhance quantum fluctuations.

B. Magnetic susceptibility

The magnetic susceptibilities (χ) of $\text{Ba}_2\text{CuTe}_{1-x}\text{W}_x\text{O}_6$ ($x = 0.00 - 0.30$) were measured in an external magnetic field of $\mu_0 H = 0.5$ T, as plotted in Fig. 4(a). As the temperature is lowered, $\chi(T)$ forms a broad maximum at around $T_{\text{max}} \sim 72$ K for $x = 0$, indicating the development of short-range correlations associated with spin-ladder magnetism. The substantial drop of $\chi(T)$ below T_{max} points to the formation of spin-singlet correlations. Overall, our $\chi(T)$ data align well with the previous results reported by Pughe *et al.* [21]. Nonetheless, muon rotation resonance and inelastic neutron scattering have uncovered the occurrence of a long-range-ordered Néel state at $T_N \sim 14$ K [25,26]. The absence of discernible anomalies accompanying the magnetic transition

is attributed to pronounced quantum fluctuations, leading to the reduction of the ordered magnetic moment, as well as the powder average of $\chi(T)$. The W^{6+} -substituted samples display a similar broad maximum, while the maximum temperature is systematically reduced from $T_{\text{max}} = 72$ K at $x = 0$ to 62 K at $x = 0.3$ [see the inset of Fig. 4(a)].

Tracing the change in $\chi(T)$ induced by W^{6+} substitution, we plot the subtracted magnetic susceptibility $\Delta\chi(x, T) = \chi(x, T) - \chi(x = 0, T) - C/T$ in Fig. 4(b). Here, C/T presents a Curie tail in the low-temperature $\chi(x, T)$, arising from defects and magnetic impurities that do not participate in the exchange coupling with the rest of the material. For the $x = 0.3$ sample, the orphan spin concentration is estimated to be $\sim 1.5\%$. Below T_{max} , an additional contribution to $\Delta\chi(x, T)$ emerges, peaking around 25 K. $\Delta\chi(x, T)$ initially shows a slight decrease at $x = 0.05$, followed by a gradual increase up to 0.2, and eventually saturates at $x = 0.3$. The peak temperature experiences a slight softening with increasing x . Our $\chi(T, x)$ data suggest that the introduction of W^{6+} ions leads to the creation of additional low-lying excitations, reflecting modulations of the spin-ladder topology.

To extract the magnetic parameters as a function of composition, the $\chi(T, x)$ data at $T = 200 - 300$ K were fitted using the Curie-Weiss law, as illustrated in Fig. 4(c):

$$\chi(T) = C/(T - \theta_{\text{CW}}) + \chi_0,$$

where C represents the Curie constant, θ_{CW} denotes the Curie-Weiss (CW) temperature, and χ_0 ($\approx 10^{-5} - 10^{-6}$ emu/mol ion) is the diamagnetic susceptibility. As plotted in Figs. 4(d) and 4(e), the magnitude of the CW temperature increases from $\theta_{\text{CW}} = -140$ to -160 K with an increasing level of W^{6+} ions. On a qualitative level, this trend is consistent with the increased strength of J_{SE} involving Cu-O-W-O-Cu pathways, while the other interactions are less significantly affected. The random activation of J_{SE} within the spin ladders generates a low-lying density of states, thereby filling up the in-gap states. This exchange randomness generated in spin-ladder geometry provides a rationale for the enhanced low-temperature $\Delta\chi(x, T)$ as shown Fig. 4(b). At the same time, the effective magnetic moment $\mu_{\text{eff}} \sim 2.19 \mu_{\text{B}}$ per Cu^{2+} shows a tendency to increase with increasing x .

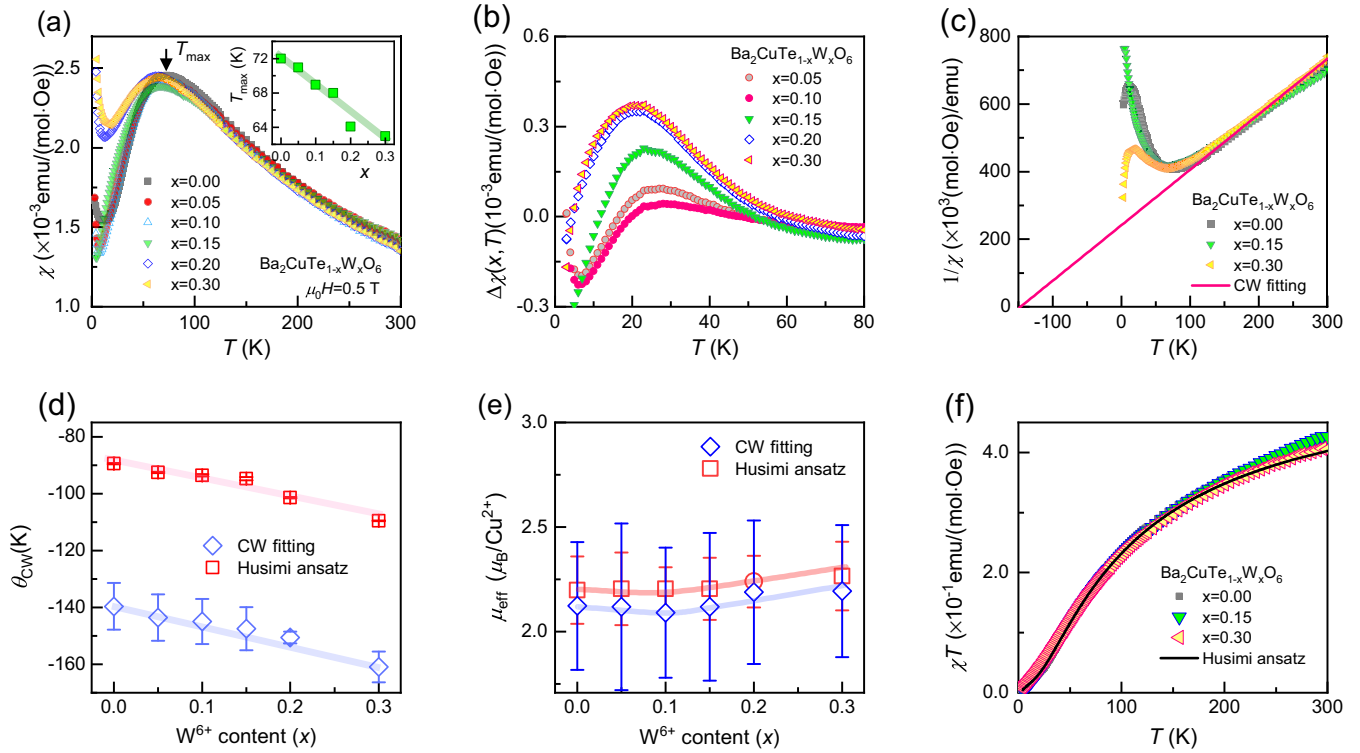


FIG. 4. (a) dc magnetic susceptibilities $\chi(T)$ of $\text{Ba}_2\text{CuTe}_{1-x}\text{W}_x\text{O}_6$ ($x = 0.00$ – 0.30) measured in an external magnetic field of $\mu_0 H = 0.5$ T. The vertical arrow indicates the temperature T_{\max} , at which $\chi(x, T)$ attains its maximum value. The inset plots T_{\max} vs x . (b) Subtracted magnetic susceptibility $\Delta\chi(x, T) = \chi(x, T) - \chi(x = 0, T) - C/T$ as a function of x and temperature. The last term represents a Curie upturn. (c) Representative $1/\chi(T)$ vs T data for $x = 0, 0.15$, and 0.3 . The solid line denotes the Curie-Weiss fitting curve. (d) Curie-Weiss temperature θ_{CW} vs x , deduced from the Curie-Weiss fit (blue diamonds) and the Husimi ansatz fit (red squares). (e) Effective magnetic moment μ_{B} vs x , which are extracted from the Curie-Weiss fit (blue diamonds) and the Husimi ansatz analysis (red squares). (f) Reduced magnetic susceptibilities χT along with the representative fit based on a Husimi ansatz.

Given the narrow fitting range of $T = 200 - 300$ K in the CW analysis, we reexamine the extracted magnetic parameters using the empirical Husimi ansatz for the reduced susceptibility χT [33],

$$\chi T = \frac{1 + b_1 \exp\left(\frac{C_1}{T}\right)}{a + b_2 \exp\left(\frac{C_2}{T}\right)},$$

where the Curie constant and the CW temperature are given by $C = (1 + b_1)/(a + b_2)$ and $\theta_{\text{CW}} = b_1 c_1 / (1 + b_1) - b_2 c_2 / (a + b_2)$, respectively. Figure 4(f) presents a representative fit using this model. As exhibited in Figs. 4(e) and 4(f), the magnitude of the CW temperature increases from $\theta_{\text{CW}} = -89.5$ to -109.6 K, while the effective magnetic moment $\mu_{\text{eff}} \sim 2.12 \mu_{\text{B}}$ increases to $\mu_{\text{eff}} \sim 2.19 \mu_{\text{B}}$ at $x = 0.3$. We find that the magnetic parameters obtained from both the conventional CW and Husimi ansatz fits show the same dependence. However, the CW fit tends to overestimate the magnetic parameters, primarily because the high-temperature paramagnetic state is not fully achieved at room temperature.

C. Specific heat

By repeating the structural and magnetic characterizations of $\text{Ba}_2\text{CuTe}_{1-x}\text{W}_x\text{O}_6$ and confirming their consistency with previous work by Pughe *et al.* [21], we are prepared to delve

into the compositional dependence of low-energy magnetic excitations. For this purpose, we measured heat capacity (C_p) in the temperature range of $T = 2 - 300$ K in zero field. Figures 5(a)–5(d) present the temperature-dependent specific heat of $\text{Ba}_2\text{CuTe}_{1-x}\text{W}_x\text{O}_6$ ($x = 0.0, 0.1, 0.2$, and 0.30). We detect no discernible anomaly related to the magnetic transition. To single out the magnetic contribution C_{mag} to the total specific heat C_p , we estimate the lattice contribution C_{latt} by combining one Debye C_{Debye} and three Einstein terms C_{Einstein} :

$$C_{\text{latt}} = 9N_D R \left(\frac{T}{\theta_D}\right)^3 \int_0^{\frac{\theta_D}{T}} \frac{x^4 e^x}{(e^x - 1)^2} dx + \sum_{n=1}^3 3N_n R \left(e^{\frac{\theta_{\text{En}}}{T}}\right)^2 \frac{e^{\frac{\theta_{\text{En}}}{T}}}{(e^{\frac{\theta_{\text{En}}}{T}} - 1)^2},$$

where $x = \frac{\hbar\omega}{k_B T}$, R is the molar gas constant, θ_D represents the Debye temperature, and θ_{En} 's are the Einstein temperatures. To optimize the estimate of C_{latt} , we systematically varied the fitting temperature range from 100 K in 5 K increments, repeating the fitting procedure until the estimated C_{latt} matched the specific heat extracted from the Fisher specific heat (see below). Additionally, we ensured that the magnetic entropy derived from C_{latt} approached the expected value of $R \ln 2$ [see Figs. 5(i)–5(l)]. By doing this, the weighting factors were set to $N_D = 1$, $N_1 = 3$, $N_2 = 2.8$, and $N_3 = 3.2$, with their

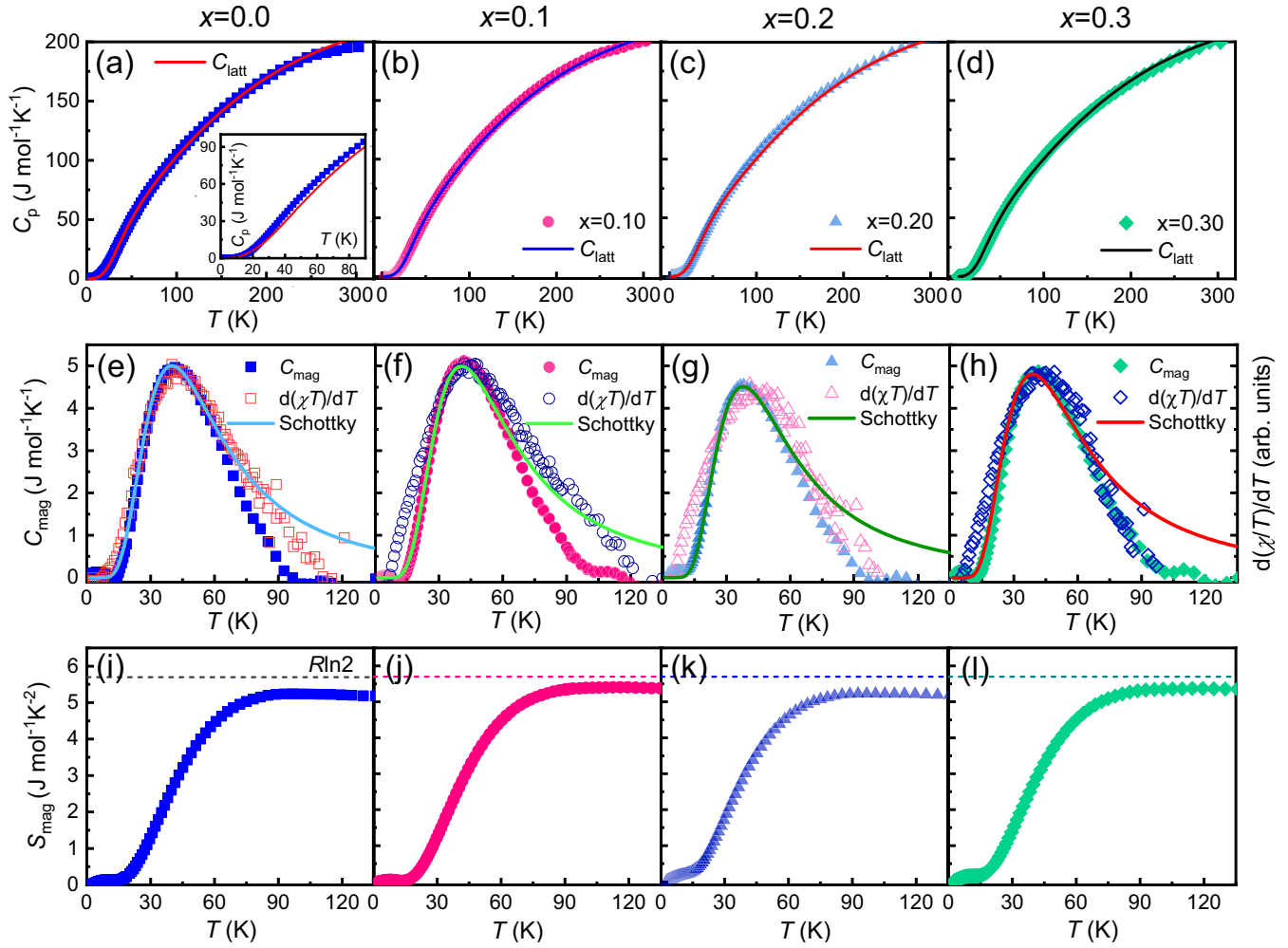


FIG. 5. Specific heat (C_p) of $\text{Ba}_2\text{CuTe}_{1-x}\text{W}_x\text{O}_6$ vs temperature for $x = 0$ (a), $x = 0.1$ (b), $x = 0.2$ (c), and $x = 0.3$ (d). The solid lines present the lattice contribution to C_p , evaluated from the Debye-Einstein model described in the main text. Comparison between the magnetic specific heat C_{mag} , obtained from the subtraction of C_p to the lattice contribution, and the Fisher specific heat $d(\chi T)/dT$, derived from the magnetic susceptibility for $x = 0$ (e), $x = 0.1$ (f), $x = 0.2$ (g), and $x = 0.3$ (h). The solid line are fitting curves to a degenerate Schottky model described in the text. The associated magnetic entropy vs temperature for $x = 0$ (i), $x = 0.1$ (j), $x = 0.2$ (k), and $x = 0.3$ (l).

sum corresponding to the total number of atoms ($N = 10$) in the chemical formula $\text{Ba}_2\text{CuTe}_{1-x}\text{W}_x\text{O}_6$. The other fitting parameters are listed in Table II. The C_{latt} contribution deviates from the total C_p below 100 K, where short-range singlet correlations start to develop. It is important to note that the Debye term simplifies the modeling of acoustic low-frequency modes, while the three Einstein terms offer the flexibility to describe three optical phonon groups at 150, 450, and 700 cm^{-1} (see the Raman spectra in Fig. 8 and compare to the Einstein temperatures in Table II). However, our adopted

TABLE II. Debye and Einstein temperatures obtained from fittings of specific-heat data to the Debye and Einstein model.

W^{6+} content	θ_D (K)	θ_{E1} (K)	θ_{E2} (K)	θ_{E3} (K)
$x = 0.00$	127	197	402	942
$x = 0.10$	132	192	390	864
$x = 0.20$	139	189	382	825
$x = 0.30$	145	186	377	786

phonon model should be considered an empirical, minimal description of C_{latt} , and the weighting coefficients used are subject to some ambiguity.

In Figs. 5(e)–5(h), $C_{\text{mag}}(T, x) [=C_p - C_{\text{latt}}]$ is plotted together with the Fisher specific heat $d(\chi T)/dT$ [34], evaluated from the magnetic susceptibilities shown in Fig. 4(a). The close overlap between $C_{\text{mag}}(T, x)$ and $d(\chi T)/dT$ validates the model employed to estimate the lattice contribution to C_p . The observed broad maximum at a temperature of approximately 40 K is reminiscent of a Schottky-like anomaly. The maximum temperature hardly varies with x . We attempted to describe $C_{\text{mag}}(T, x)$ using a degenerate Schottky model, $g(\Delta/k_B T)^2 e^{-\Delta/k_B T} / [1 + g e^{-\Delta/k_B T}]^2$, where Δ is the energy gap and g is the degeneracy ratio between two energy levels. It is apparent that deviations occur in the high- T tail ($T > 60$ K) due to the presence of interladder and three-dimensional interactions. $\Delta/k_B \sim 110\text{--}120$ K is an order of J_{leg} and $g = 4.6$ at $x = 0$ is lowered to 3.3 at $x = 0.3$. It is noteworthy that the deduced spin gap is comparable to $\Delta_R/k_B \sim 110$ K obtained from the ^{125}Te spin-lattice relaxation rate [24]. Unlike

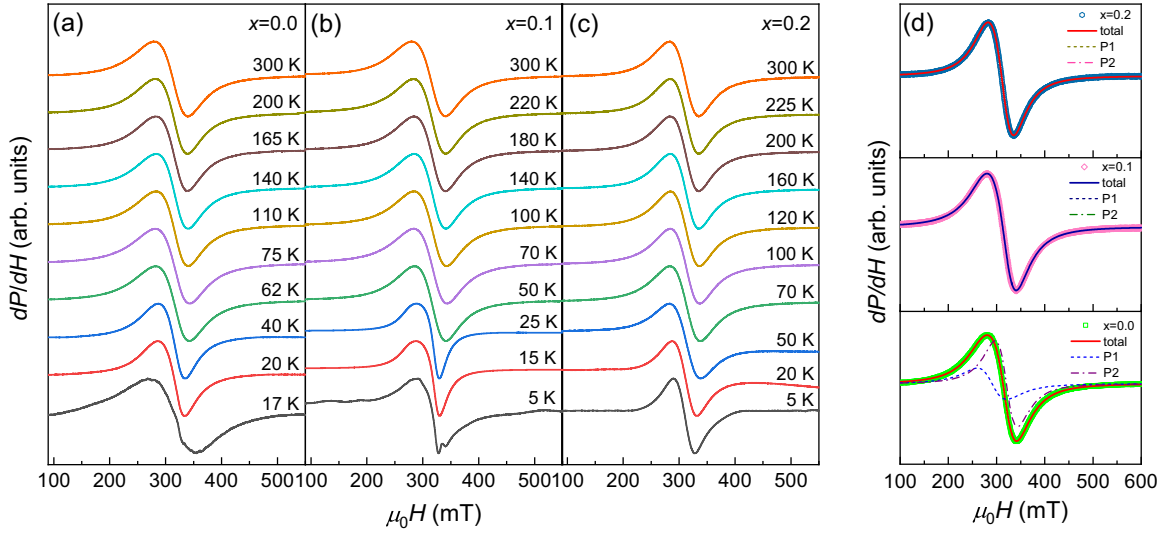


FIG. 6. Derivative of the ESR absorption spectra, dP/dH , for (a) $x = 0.0$, (b) $x = 0.1$, and (c) $x = 0.2$ as a function of temperature. The spectra are vertically shifted for clarity. (d) Representative fittings of the room-temperature dP/dH into two Lorentzian profiles: P1 (dashed line) and P2 (dot-dashed line). The solid lines represent the sum of two components.

the static magnetic susceptibility $\chi(x, T)$, $C_{\text{mag}}(T, x)$ exhibits little change with x , except that $C_{\text{mag}}(T, x)$ becomes somewhat symmetric at $x = 0.3$.

Figures 5(i)–4(l) present the magnetic entropy, $S_{\text{mag}}(T, x)$, calculated by integrating C_{mag}/T with respect to temperature. $S_{\text{mag}}(T, x)$ reaches 90% of the theoretically expected value $R \ln 2 = 5.76 \text{ J}/(\text{K mol})$ for $s = 1/2$ moments as the temperature approaches 80 K. The missing magnetic entropy is attributed to an overestimation of the actual lattice contribution. A majority of $S_{\text{mag}}(T, x)$ is released in the temperature interval of $T = 20 - 70 \text{ K}$ [$\approx T_{\text{max}}$ in Fig. 4(a)], where the magnetic susceptibility develops the short-range singlet correlations. Furthermore, the negligible entropy release below 20 K demonstrates that the magnetic ordering involves only a tiny amount of entropy. Although our lattice model captures the key features of C_{mag} , it is not sufficiently sophisticated to precisely reflect the material's phonon spectrum.

D. Electron spin resonance

The W^{6+} substitution effects on spin correlations were investigated by X-band ESR. The ESR spectra, plotted as a function of temperature, are shown in Figs. 6(a)–6(c) for $x = 0.0, 0.1$, and 0.2 , respectively. Throughout the entire measured temperatures, the powder spectra are well fitted to the deconvolution of the derivative of two Lorentzian profiles, as indicated by P1 and P2 in Fig. 6(d). The g -factors in the high- T paramagnetic regime are $g_c = 2.08$ and $g_{ab} = 2.15$ (see the insets of Fig. 7), characteristic of Cu^{2+} ions with a quenched orbital moment.

In Fig. 7, we display the extracted resonance field $H_{\text{res}}(T)$ and the peak-to-peak linewidth $\Delta H_{pp}(T)$ for the P1 and P2 peaks. We recall that the resonance field reflects the development of internal magnetic fields, while $\Delta H_{pp}(T)$, reciprocally proportional to the spin-spin relaxation rate $1/T_2^*$, bears information on spin-spin correlations. In the paramagnetic regime where $1/\chi(T)$ exhibits a linear dependence [see the solid line

in Fig. 4(c)], both $H_{\text{res}}(T)$ and $\Delta H_{pp}(T)$ are largely independent of temperature. The slight temperature dependency may be linked to the structural transition from $C2/m$ to $P1$, which occurs at approximately 280 K for $x = 0$ and 240 K for $x = 0.1$ [21]. This structural transition is challenging to quantify based on our ESR parameters.

As shown in Fig. 7(a), $H_{\text{res}}(T)$ of the P1 absorption peak shows a steep increase below approximately T_{max} [marked by the vertical arrows in Fig. 7(a)], signaling the development of spin-singlet correlations. With increasing x , the onset temperature decreases from $\sim 64 \text{ K}$ at $x = 0$ to $\sim 36 \text{ K}$ at $x = 0.2$, consistent with the weakening of the singlet correlations with increasing W^{6+} substitution. Conversely, $H_{\text{res}}(T)$ of the P2 line undergoes a substantial downshift below 30 K, as indicated by the down arrows in Fig. 7(b), in a temperature range where both C_{mag} and S_{mag} become negligibly small (see Fig. 5). The opposite thermal behavior of $H_{\text{res}}(T)$ observed in P2 is attributed to the onset of anti-ferromagnetic critical correlations, distinct from the singlet correlations.

As evident from Figs. 7(c) and 7(d), $\Delta H_{pp}(T)$ of the P1 and P2 peaks shows a similar temperature dependence. Initially, upon cooling from T_{max} , $\Delta H_{pp}(T)$ undergoes a rapid decrease, which is typical of $s = 1/2$ spin-ladder materials [35]. We stress that the ESR line narrowing takes place in the temperature interval of 25–75 K for $x = 0$, where gapped singletlike excitations dominate [24]. In spin systems with gapped triplon excitations, the ESR linewidth is dictated by the inverse lifetime of triplets. As the temperature decreases below the effective energy gap, the population of triplets becomes more diluted, leading to an increase in their lifetime (T_2^*). This explains the observed narrowing of the ESR absorption with decreasing temperature. We stress that essentially the same behavior was observed in the coupled two-leg spin ladder $\text{Ba}_2\text{CuTeO}_6$, which features spin-gap excitations and long-range magnetic ordering at 15 K [25].

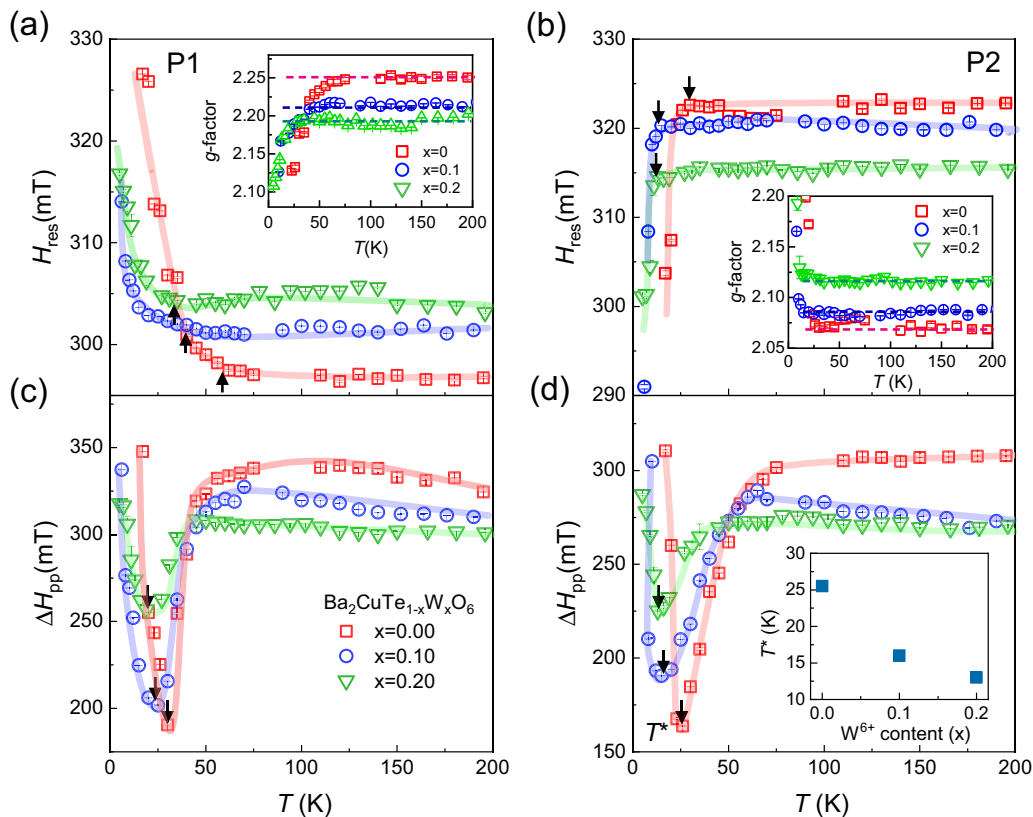


FIG. 7. Temperature dependence of the resonance field $H_{\text{res}}(T)$ for (a) P1 and (b) P2 peaks with $x = 0$ (red squares), $x = 0.1$ (blue circles), and $x = 0.2$ (green inverse triangles). The insets plot g -factors vs temperature. The vertical arrows denote the onset temperature of the shift in $H_{\text{res}}(T)$. Temperature dependence of the peak-to-peak linewidth $\Delta H_{pp}(T)$ for (c) P1 and (d) P2 peaks. The vertical arrows mark the characteristic temperatures T^* where the ESR linewidth exhibits a minimum. The inset plots T^* vs x . The opaque thick lines are a guide to the eye.

Remarkably, the upturn of $\Delta H_{pp}(T)$ at T^* is closely linked with the downshift of $H_{\text{res}}(T)$ for the P2 peak. In this vein, the characteristic temperature T^* can be taken as an indicator of a critical slowing down, reflecting the divergent correlation length on approaching the magnetic transition temperature. The critical line broadening typically follows a power-law increase. However, reliable fittings could not be conducted due to the narrow temperature window available. The upturn temperature T^* decreases from 26 K at $x = 0.0$ to 13 K at $x = 0.2$ [see the inset of Fig. 7(d)], while the associated dip becomes shallower. From our ESR observations, we infer that the long-range transition temperature is lowered below 5 K for $x = 0.2$, and the spin-ladder-like correlations are weakened as a result of changes in the spin topology induced by the W^{6+} substitution. As evident from Fig. 6(c), the $T = 5$ K ESR spectrum of the $x = 0.2$ sample shows no distorted features, unlike the corresponding spectrum of the $x = 0.1$ sample [Fig. 6(b)], providing circumstantial evidence for the absence of long-range magnetic ordering down to 5 K. Future μ SR investigations are called for to determine the exact critical temperature for compositions above $x = 0.2$.

E. Raman scattering

We now turn our attention to low-lying magnetic excitations probed through double spin-flip processes by Raman

spectroscopy. Figure 8 compares the Raman spectra of $\text{Ba}_2\text{CuTe}_{1-x}\text{W}_x\text{O}_6$ ($x = 0.00, 0.10, \text{ and } 0.20$). At a base temperature of $T = 5$ K, we were able to identify 23 A_g phonon peaks in the frequency range of $15\text{--}800\text{ cm}^{-1}$, which is somewhat lower than the expected 27 A_g one-phonon Raman-active modes for the triclinic \bar{P} structure. The missing modes are ascribed to either a lack of phonon intensity or their overlap with other phonons, particularly true for pellets. We find no significant changes in the phonon frequencies and the number of phonon modes as a function of x . As such, our following analysis will concentrate on the magnetic continuum observed around 150 cm^{-1} , as highlighted by colored shadings in Figs. 8(a)–8(c).

Figures 8(d)–8(f) present the color contour plots of the magnetic Raman scattering intensity in the temperature-frequency (T - ω) plane. In spin-gapped (antiferromagnetically ordered) systems, elementary excitations are given by triplons (magnons). In the context of spin-conserving Raman scattering processes, two-triplon (two-magnon) excitations provide a major scattering channel [36–39]. Our ESR data show a crossover from antiferromagnetic to spin-ladder-like correlations across T_N . As such, the two-paramagnon excitations may acquire characteristics of triplon excitations at elevated temperatures.

First, we are able to deduce the exchange interaction strength of $J \approx 80$ K from the peak energy $\omega_{2M} \sim 150\text{ cm}^{-1}$

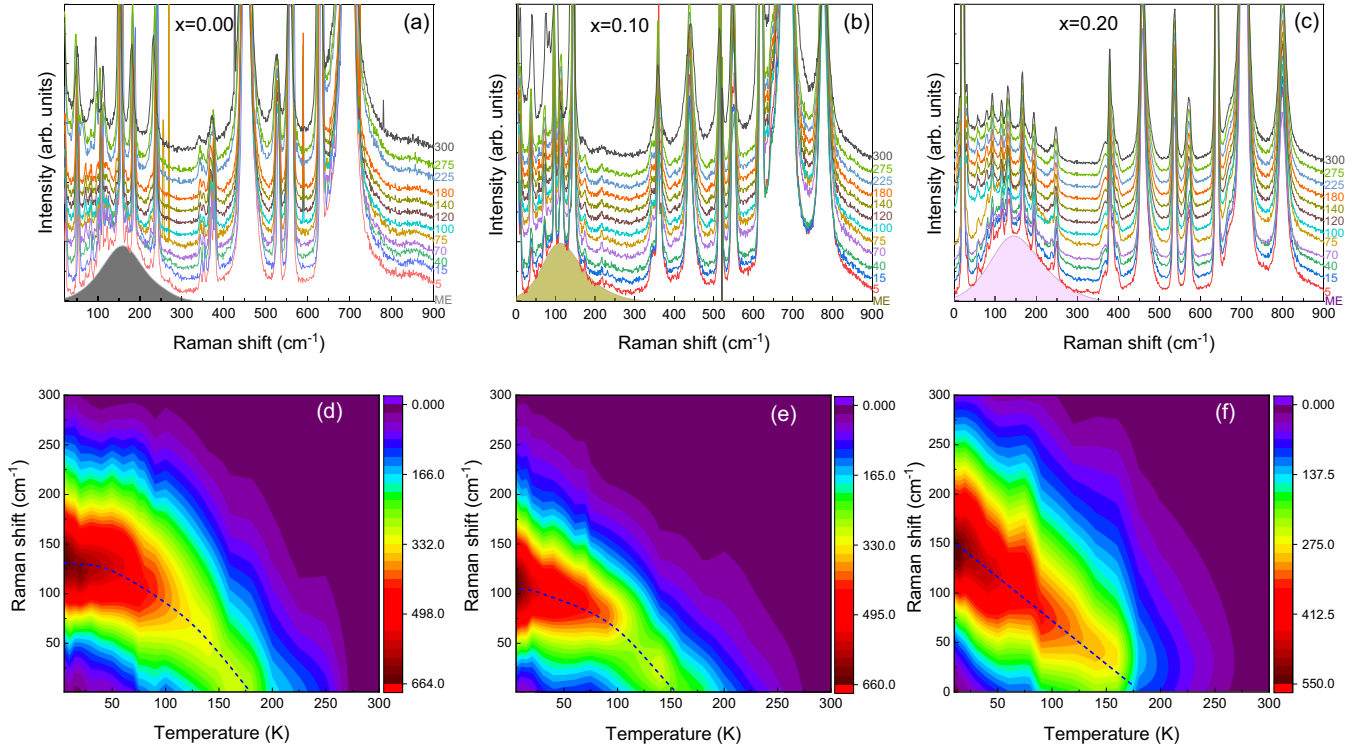


FIG. 8. Temperature dependence of Raman spectra of $\text{Ba}_2\text{CuTe}_{1-x}\text{W}_x\text{O}_6$ measured in cross-polarization for (a) $x = 0.00$, (b) $x = 0.10$, and (c) $x = 0.20$. The spectra are vertically offset by a constant amount for clarity. The color shadings mark magnetic excitations. The color contour of the associated magnetic Raman scattering intensity in temperature vs Raman shift is plotted for (d) $x = 0.00$, (e) $x = 0.10$, and (f) $x = 0.20$. The dashed lines are guides to the eye for the peak positions.

of the two-magnon continuum. This estimation is based on the relation $\omega_{2M} \approx 2.7 J$, which is established for $s = 1/2$ two-dimensional antiferromagnets [34]. In this regard, the actual exchange interaction is somewhat underestimated for our coupled spin ladders, whose effective dimensionality is less than $d = 2$. In addition, averaging the two-magnon spectrum over a powder sample introduces additional uncertainties. Based on the spectral shape and energy alone, it remains challenging to determine whether there is a substantial change in the exchange topology.

Second, the observed thermal damping and softening of the two-magnon excitations are not typical of conventional magnon behavior. In the case of conventional antiferromagnets, magnons are strongly renormalized and damped as the temperature approaches T_N . For $x = 0$, T_{max} appears to provide the characteristic temperature scale for the thermal behavior of quasiparticle excitations, as guided by the dashed line in Fig. 8(d). Thus, the temperature dependence of magnetic excitations is set by spin-singlet correlations pertinent to triplonlike excitations. With increasing x , a quasilinear behavior of thermal softening becomes evident, implying that the simple magnon and triplon picture is insufficient to explain the intriguing spin dynamics. As the magnetic ordering is suppressed upon the introduction of W^{6+} ions, the quasiparticle excitations are subject to enhanced quantum-critical fluctuations.

Taking all the collected data into account, the impact of d^{10}/d^0 substitution on the spin-ladder compounds $\text{Ba}_2\text{CuTe}_{1-x}\text{W}_x\text{O}_6$ appears moderate when compared to the

more pronounced effects observed in the double perovskite structure $\text{Sr}_2\text{Cu}(\text{Te}_{1-x}\text{W}_x)\text{O}_6$. In the latter, the Néel ordered state is destabilized as soon as W^{6+} ions are introduced [11]. For the studied compound, both the $\chi(T)$ and ESR data reveal a gradual weakening of spin-ladder magnetism with increasing W^{6+} content, pointing to delicate modifications of the original spin Hamiltonian. Pughe *et al.* [21] interpreted this as an enhancement of J_{leg} over J_{rung} , favoring one-dimensional magnetism. Alternatively, the newly generated J_{SE} interaction [see the sketch in Fig. 1(b)] induces spin tetrahedra, zero-dimensional frustrated spin clusters, disrupting the uniformity of the coupled spin ladder. This provides a qualitative explanation for the observed decrease in T_N , the in-gap-like emergent magnetic susceptibility below the temperature T_{max} , and the increase in the Curie-Weiss temperature. In the case of a square-lattice Heisenberg J_1 - J_2 model, an amplified J_2 relative to J_1 influences the entire lattice, thereby destabilizing rapidly a long-range order. In sharp contrast, the J_{SE} interaction, enabled through the Cu-O-W-O-Cu path, primarily affects intraladder magnetism. Consequently, its influence is predominantly localized in the case of quasi-one-dimensional spin ladders, with less effect on the overall lattice.

IV. CONCLUSIONS

To conclude, we have investigated the impact of chemical substitution on magnetic characteristics in spin-ladder compounds $\text{Ba}_2\text{CuTe}_{1-x}\text{W}_x\text{O}_6$. For the pristine sample, magnetic susceptibility exhibiting a broad maximum $T_{\text{max}} \sim 70$ K,

Schottky-like specific heat, unconventional magnetic Raman scattering, and a quasilinear decrease in the ESR linewidth provides compelling evidence of dominant spin-singlet correlations at elevated temperatures that evolve into antiferromagnetic ordering at low temperatures. Singularly, the W-for-Te substitution induces notable changes: an increase in the Curie-Weiss temperature, a decrease in the Néel ordering temperature, an increased low-temperature magnetic susceptibility, and a weakening of spin-ladder correlations. These observations collectively suggest that the incorporation of W^{6+} ions enables additional exchange inter-

actions, which mainly modify the intraladder spin topology. Our extensive analysis demonstrates that the W substitution pushes $Ba_2CuTe_{1-x}W_xO_6$ towards a quantum-critical regime, showcasing the intriguing tuning of magnetic properties in spin-ladder systems.

ACKNOWLEDGMENTS

This work was supported by the National Research Foundation (NRF) of Korea (Grants No. NRF-2020R1A5A1016518, No. RS-2023-00209121, and No. RS-2023-00214312).

APPENDIX

1. Rietveld refinement results for the powder x-ray data on $Ba_2CuTe_{1-x}W_xO_6$

Tables III–VI provide the structural information obtained from the Rietveld refinement of the powder x-ray diffraction data at room temperature for Ba_2CuTeO_6 , $Ba_2CuTe_{0.9}W_{0.1}O_6$, $Ba_2CuTe_{0.8}W_{0.2}O_6$, and $Ba_2CuTe_{0.7}W_{0.3}O_6$, respectively. All four compositions crystallize in the crystal structure of the space group $C2/m$.

TABLE III. Structural information extracted from the Rietveld refinement of the powder x-ray diffraction data at 300 K of Ba_2CuTeO_6 .

Ba_2CuTeO_6						
Space Group: $C2/m$, No. 12, 300 K						
$R_p = 0.0856$, $R_{wp} = 0.1116$, $R_{exp} = 0.0740$, $\chi^2 = 2.279$, RF-factor = 0.135						
$a = 10.2288(2) \text{ \AA}$, $b = 5.7213(2) \text{ \AA}$, $c = 10.0931(7) \text{ \AA}$, $\beta = 107.99(8)^\circ$, $V = 561.7726(9) \text{ \AA}^3$						
Atom	Wyckoff Position	X	Y	Z	Occ	
Ba ₁	4i	0.1263	0	0.3786	1	
Ba ₂	4i	0.2851	0	0.8506	1	
Cu	4i	-0.0949	0.5	0.2097	1	
Te ₁	2a	0	0	0	1	
Te ₂	2d	0	0.5	0.5	0.98(3)	
O ₁	4i	0.1756	0.5	0.4007	1	
O ₂	8j	-0.0499	0.5034	0.3731	1	
O ₃	4i	0.2955	0.5	0.9068	1	
O ₄	8j	0.0473	0.7349	0.8620	1	

TABLE IV. Structural information extracted from the Rietveld refinement of the powder x-ray diffraction data at 300 K of $Ba_2CuTe_{0.9}W_{0.1}O_6$.

$Ba_2CuTe_{0.9}W_{0.1}O_6$						
Space Group: $C2/m$, No. 12, 300 K						
$R_p = 0.0545$, $R_{wp} = 0.0742$, $R_{exp} = 0.0406$, $\chi^2 = 3.335$, RF-factor = 0.0785						
$a = 10.2244(2) \text{ \AA}$, $b = 5.7191(5) \text{ \AA}$, $c = 10.091(6) \text{ \AA}$, $\beta = 107.960(3)^\circ$, $V = 561.3506(1) \text{ \AA}^3$						
Atom	Wyckoff Position	X	Y	Z	Occ	
Ba ₁	4i	0.1296	0	0.3794	1	
Ba ₂	4i	0.2834	0	0.8500	1	
Cu	4i	-0.0936	0.5	0.2143	1	
Te ₁	2a	0	0	0	0.8494	
W ₁	2a	0	0	0	0.1330	
Te ₂	2d	0	0.5	0.5	0.8448	
W ₂	2d	0	0.5	0.5	0.0710	
O ₁	4i	0.1427	0.5	0.3991	1	
O ₂	8j	-0.1114	0.7474	0.3697	1	
O ₃	4i	0.3172	0.5	0.8718	1	
O ₄	8j	0.0497	0.7606	0.8891	1	

TABLE V. Structural information extracted from the Rietveld refinement of the powder x-ray diffraction data at 300 K of $\text{Ba}_2\text{CuTe}_{0.8}\text{W}_{0.2}\text{O}_6$.

$\text{Ba}_2\text{CuTe}_{0.8}\text{W}_{0.2}\text{O}_6$					
Space Group: $C2/m$, No. 12, 300 K					
$R_p = 0.0583$, $R_{wp} = 0.0800$, $R_{exp} = 0.0418$, $\chi^2 = 3.676$, RF-factor = 0.1134					
$a = 10.2162(5)\text{Å}$, $b = 5.7160(1)\text{Å}$, $c = 10.0869(7)\text{Å}$, $\beta = 107.928(3)^\circ$, $V = 560.4382(9)\text{Å}^3$					
Atom	Wyckoff Position	X	Y	Z	Occ
Ba ₁	4i	0.1302	0	0.3790	1
Ba ₂	4i	0.2838	0	0.8502	1
Cu	4i	-0.0952	0.5	0.2132	1
Te ₁	2a	0	0	0	0.80
W ₁	2a	0	0	0	0.20
Te ₂	2d	0	0.5	0.5	0.80
W ₂	2d	0	0.5	0.5	0.20
O ₁	4i	0.1312	0.5	0.4024	1
O ₂	8j	-0.1012	0.7244	0.3706	1
O ₃	4i	0.3215	0.5	0.8762	1
O ₄	8j	0.0492	0.7590	0.8928	1

TABLE VI. Structural information extracted from the Rietveld refinement of the powder x-ray diffraction data at 300 K of $\text{Ba}_2\text{CuTe}_{0.7}\text{W}_{0.3}\text{O}_6$.

$\text{Ba}_2\text{CuTe}_{0.7}\text{W}_{0.3}\text{O}_6$					
Space Group: $C2/m$, No. 12, 300 K					
$R_p = 0.0559$, $R_{wp} = 0.0760$, $R_{exp} = 0.0402$, $\chi^2 = 3.569$, RF-factor = 0.0682					
$a = 10.21268(3)\text{Å}$, $b = 5.71580(6)\text{Å}$, $c = 10.08562(3)\text{Å}$, $\beta = 107.92666(6)^\circ$, $V = 560.1528(4)\text{Å}^3$					
Atom	Wyckoff Position	X	Y	Z	Occ
Ba ₁	4i	0.1296	0	0.3804	1
Ba ₂	4i	0.2847	0	0.8499	1
Cu	4i	-0.0939	0.5	0.2129	1
Te ₁	2a	0	0	0	0.7020
W ₁	2a	0	0	0	0.3026
Te ₂	2d	0	0.5	0.5	0.6940
W ₂	2d	0	0.5	0.5	0.30
O ₁	4i	0.1563	0.5	0.4006	1
O ₂	8j	-0.1163	0.7445	0.3693	1
O ₃	4i	0.3115	0.5	0.8727	1
O ₄	O	0.0360	0.7580	0.8845	1

- [1] S. Maekawa, Superconductivity in spin ladders, *Science* **273**, 1515 (1996).
- [2] M. Uehara, T. Nagata, J. Akimitsu, H. Takahashi, N. Mori, and K. Kinoshita, Superconductivity in the ladder material $\text{Sr}_{0.4}\text{Ca}_{13.6}\text{Cu}_{24}\text{O}_{41.84}$, *J. Phys. Soc. Jpn.* **65**, 2764 (1996).
- [3] B. Thielemann, C. Rüegg, H. M. Rønnow, A. M. Läuchli, J.-S. Caux, B. Normand, D. Biner, K. W. Krämer, H.-U. Güdel, J. Stahn, K. Habicht, K. Kiefer, M. Boehm, D. F. McMorrow, and J. Mesot, Direct observation of magnon fractionalization in the quantum spin ladder, *Phys. Rev. Lett.* **102**, 107204 (2009).
- [4] M. Jeong, H. Mayaffre, C. Berthier, D. Schmidiger, A. Zheludev, and M. Horvatic, Attractive Tomonaga-Luttinger liquid in a quantum spin ladder, *Phys. Rev. Lett.* **111**, 106404 (2013).
- [5] K.-Y. Choi, J. W. Hwang, P. Lemmens, D. Wulferding, G. J. Shu, and F. C. Chou, Evidence for dimer crystal melting in the frustrated spin-ladder system BiCu_2PO_6 , *Phys. Rev. Lett.* **110**, 117204 (2013).
- [6] S. R. White, R. M. Noack, and D. J. Scalapino, Resonating valence bond theory of coupled Heisenberg chains, *Phys. Rev. Lett.* **73**, 886 (1994).
- [7] D. Iwanaga, Y. Inaguma, and M. Itoh, Crystal structure and magnetic properties of B-site ordered perovskite-type oxides $\text{A}_2\text{CuB}'\text{O}_6$ ($\text{A} = \text{Ba}, \text{Sr}$; $\text{B}' = \text{W}, \text{Te}$), *J. Solid State Chem.* **147**, 291 (1999).

- [8] S. Vasala and M. Karppinen, $A_2B'B''O_6$ perovskites: a review, *Prog. Solid State Chem.* **43**, 1 (2015).
- [9] V. M. Katukuri, P. Babkevich, O. Mustonen, H. C. Walker, B. Fåk, S. Vasala, M. Karppinen, H. M. Rønnow, and O. V. Yazyev, Exchange interactions mediated by nonmagnetic cations in double perovskites, *Phys. Rev. Lett.* **124**, 077202 (2020).
- [10] Y. Xu, S. Liu, N. Qu, Y. Cui, Q. Gao, R. Chen, J. Wang, F. Gao, and X. Hao, Comparative description of magnetic interactions in Sr_2CuTeO_6 and Sr_2CuWO_6 , *J. Phys.: Condens. Matter* **29**, 105801 (2017).
- [11] O. Mustonen, S. Vasala, E. Sadrollahi, K. P. Schmidt, C. Baines, H. C. Walker, I. Terasaki, F. J. Litterst, E. Baggio-Saitovitch, and M. Karppinen, Spin-liquid-like state in a spin-1/2 square-lattice antiferromagnet perovskite induced by $d^{10}-d^0$ cation mixing, *Nat. Commun.* **9**, 1085 (2018).
- [12] O. Mustonen, S. Vasala, K. P. Schmidt, E. Sadrollahi, H. C. Walker, I. Terasaki, F. J. Litterst, E. Baggio-Saitovitch, and M. Karppinen, Tuning the square-lattice antiferromagnet from Néel order to quantum disorder to columnar order, *Phys. Rev. B* **98**, 064411 (2018).
- [13] O. H. J. Mustonen, C. E. Pughe, H. C. Walker, H. M. Mutch, G. B. G. Stenning, F. C. Coomer, and E. J. Cussen, Diamagnetic d-orbitals drive magnetic structure selection in the double perovskite Ba_2MnTeO_6 , *Chem. Mater.* **32**, 7070 (2020).
- [14] T. Koga, N. Kurita, M. Avdeev, S. Danilkin, T. J. Sato, and H. Tanaka, Magnetic structure of the $S = 1/2$ quasi-two-dimensional square-lattice Heisenberg antiferromagnet Sr_2CuTeO_6 , *Phys. Rev. B* **93**, 054426 (2016).
- [15] P. Babkevich, V. M. Katukuri, B. Fåk, S. Rols, T. Fennell, D. Pajic, H. Tanaka, T. Pardini, R. R. P. Singh, A. Mitrushchenkov, O. V. Yazyev, and H. M. Rønnow, Magnetic excitations and electronic interactions in Sr_2CuTeO_6 : A spin-1/2 square lattice Heisenberg antiferromagnet, *Phys. Rev. Lett.* **117**, 237203 (2016).
- [16] H. C. Walker, O. Mustonen, S. Vasala, D. J. Voneshen, M. D. Le, D. T. Adroja, and M. Karppinen, Spin wave excitations in the tetragonal double perovskite Sr_2CuWO_6 , *Phys. Rev. B* **94**, 064411 (2016).
- [17] M. Watanabe, N. Kurita, H. Tanaka, W. Ueno, K. Matsui, and T. Goto, Valence-bond-glass state with a singlet gap in the spin-1/2 square-lattice random $J_1 - J_2$ Heisenberg antiferromagnet $Sr_2CuTe_{1-x}W_xO_6$, *Phys. Rev. B* **98**, 054422 (2018).
- [18] S. Yoon, W. Lee, S. Lee, J. Park, C. H. Lee, Y. S. Choi, S.-H. Do, W.-J. Choi, W.-T. Chen, F. C. Chou, D. I. Gorbunov, Y. Oshima, A. Ali, Y. Singh, A. Berlie, I. Watanabe, and K.-Y. Choi, Quantum disordered state in the $J_1 - J_2$ square-lattice antiferromagnet $Sr_2Cu(Te_{0.95}W_{0.05})O_6$, *Phys. Rev. Mater.* **5**, 014411 (2021).
- [19] W. Hong, L. Liu, C. Liu, X. Ma, A. Koda, X. Li, J. Song, W. Yang, J. Yang, P. Cheng, H. Zhang, W. Bao, X. Ma, D. Chen, K. Sun, W. Guo, H. Luo, A. W. Sandvik, and S. Li, Extreme suppression of antiferromagnetic order and critical scaling in a two-dimensional random quantum magnet, *Phys. Rev. Lett.* **126**, 037201 (2021).
- [20] O. H. J. Mustonen, E. Fogh, J. A. M. Paddison, L. Mangin-Thro, T. Hansen, H. Y. Playford, M. Diaz-Lopez, P. Babkevich, S. Vasala, M. Karppinen, E. J. Cussen, H. M. Rønnow, and H. C. Walker, Structure, spin correlations, and magnetism of the $S = 1/2$ square-lattice antiferromagnet $Sr_2CuTe_{1-x}W_xO_6$ ($0 \leq x \leq 1$), *Chem. Mater.* **36**, 501 (2024).
- [21] C. Pughe, O. H. J. Mustonen, A. S. Gibbs, M. Etter, C. Liu, S. E. Dutton, A. Friskney, N. C. Hyatt, G. B. G. Stenning, H. M. Mutch, F. C. Coomer, and E. J. Cussen, Site-selective d^{10}/d^0 substitution in an $S = 1/2$ spin ladder $Ba_2CuTe_{1-x}W_xO_6$ ($0 \leq x \leq 0.3$), *Inorg. Chem.* **61**, 4033 (2022).
- [22] P. Köhl and D. Reinen, Strukturelle und spektroskopische Untersuchungen am Ba_2CuTeO_6 , *Z. Anorg. Allg. Chem.* **409**, 257 (1974).
- [23] G. N. Rao, R. Sankar, A. Singh, I. P. Muthuselvam, W. T. Chen, V. N. Singh, G.-Y. Guo, and F. C. Chou, Tellurium-bridged two-leg spin ladder in Ba_2CuTeO_6 , *Phys. Rev. B* **93**, 104401 (2016).
- [24] A. S. Gibbs, A. Yamamoto, A. N. Yaresko, K. S. Knight, H. Yasuoka, M. Majumder, M. Baenitz, P. J. Saines, J. R. Hester, D. Hashizume, A. Kondo, K. Kindo, and H. Takagi, $S = 1/2$ quantum critical spin ladders produced by orbital ordering in Ba_2CuTeO_6 , *Phys. Rev. B* **95**, 104428 (2017).
- [25] A. Glamazda, Y. S. Choi, S.-H. Do, S. Lee, P. Lemmens, A. N. Ponomaryov, S. A. Zvyagin, J. Wosnitza, Dita Puspita Sari, I. Watanabe, and K.-Y. Choi, Quantum criticality in the coupled two-leg spin ladder Ba_2CuTeO_6 , *Phys. Rev. B* **95**, 184430 (2017).
- [26] D. Macdougall, A. S. Gibbs, T. Ying, S. Wessel, H. C. Walker, D. Voneshen, F. Mila, H. Takagi, and R. Coldea, Spin dynamics of coupled spin ladders near quantum criticality in Ba_2CuTeO_6 , *Phys. Rev. B* **98**, 174410 (2018).
- [27] Y. Todate, Antiferromagnetism and frustration in Ba_2CuWO_6 , *J. Phys. Soc. Jpn.* **70**, 337 (2001).
- [28] O. Mustonen, S. Vasala, H. Mutch, C. I. Thomas, G. B. G. Stenning, E. Baggio-Saitovitch, E. J. Cussen, and M. Karppinen, Magnetic interactions in the $S = 1/2$ square-lattice antiferromagnets Ba_2CuTeO_6 and Ba_2CuWO_6 : Parent phases of a possible spin liquid, *Chem. Commun.* **55**, 1132 (2019).
- [29] Y. C. Chung, S. K. Karna, F. C. Chou, and H. L. Liu, Electronic structure and lattice dynamics of Ba_2CuTeO_6 single crystals, *RSC Adv.* **10**, 20067 (2020).
- [30] S. K. Pradhan, R. Datta, and S. Kumar De, Effect of Ru substitution in tellurium bridged copper spin 1/2 system Ba_2CuTeO_6 : Structure, magnetism and optical properties, *J. Phys. Chem. Solids* **156**, 110129 (2021).
- [31] C. Pughe, O. H. J. Mustonen, A. S. Gibbs, S. Lee, R. Stewart, B. Gade, C. Wang, H. Huetkens, A. Forster, F. C. Coomer, H. Takagi, and E. J. Cussen, Partitioning the two-leg spin ladder in $Ba_2Cu_{1-x}Zn_xTeO_6$: From magnetic order through spin-freezing to paramagnetism, *Chem. Mater.* **35**, 2752 (2023).
- [32] L. B. McCusker, R. B. von Dreele, D. E. Cox, D. Louër, and P. Scardi, Rietveld refinement guidelines, *J. Appl. Cryst.* **32**, 36 (1999).
- [33] R. Pohle and L. D. C. Jaubert, Curie-Weiss crossover in spin liquids, *Phys. Rev. B* **108**, 024411 (2023).
- [34] M. E. Fisher, Relation between the specific heat and susceptibility of an antiferromagnet, *Philos. Mag. A: J. Theor. Exp. Appl. Phys.* **7**, 1731 (1962).
- [35] A. N. Ponomaryov, M. Ozerov, L. Zviagina, J. Wosnitza, K. Y. Povarov, F. Xiao, A. Zheludev, C. Landee, E. Čížmár, A. A. Zvyagin, and S. A. Zvyagin, Electron spin resonance in a

- strong rung spin-1/2 Heisenberg ladder, [Phys. Rev. B **93**, 134416 \(2016\)](#).
- [36] K. B. Lyons, P. A. Fleury, J. P. Remeika, A. S. Cooper, and T. J. Negran, Dynamics of spin fluctuations in lanthanum cuprate, [Phys. Rev. B **37**, 2353 \(1988\)](#).
- [37] M. G. Cottam and D. J. Lockwood, *Light Scattering in Magnetic Solids* (Wiley, New York, 1986).
- [38] D. Wulferding, Y. Choi, W. Lee, and K.-Y. Choi, Raman spectroscopic diagnostic of quantum spin liquids, [J. Phys.: Condens. Matter **32**, 043001 \(2020\)](#).
- [39] K.-Y. Choi, A. Oosawa, H. Tanaka, and P. Lemmens, Interplay of triplets and lattice degrees of freedom in the coupled spin dimer system KCuCl_3 , [Phys. Rev. B **72**, 024451 \(2005\)](#).